Front. Mech. Eng. 2020, 15(3): 374–389
https://doi.org/10.1007/s11465-019-0580-8

RESEARCH ARTICLE

Jin ZENG, Chenguang ZHAO, Hui MA, Bangchun WEN

Dynamic modeling and coupling characteristics of rotating inclined beams with twisted-shape sections

Abstract In the existing literature, most studies investigated the free vibrations of a rotating pre-twisted cantilever beam; however, few considered the effect of the elastic-support boundary and the quantification of modal coupling degree among different vibration directions. In addition, Coriolis, spin softening, and centrifugal stiffening effects are not fully included in the derived equations of motion of a rotating beam in most literature, especially the centrifugal stiffening effect in torsional direction. Considering these deficiencies, this study established a coupled flapwise–chordwise–axial–torsional dynamic model of a rotating double-tapered, pre-twisted, and inclined Timoshenko beam with elastic supports based on the semi-analytic method. Then, the proposed model was verified with experiments and ANSYS models using Beam188 and Shell181 elements. Finally, the effects of setting and pre-twisted angles on the degree of coupling among flapwise, chordwise, and torsional directions were quantified via modal strain energy ratios. Results showed that 1) the appearance of torsional vibration originates from the combined effect of flapwise–torsional and chordwise–torsional couplings dependent on the Coriolis effect, and that 2) the flapwise–chordwise coupling caused by the pure pre-twisted angle is stronger than that caused by the pure setting angle.

Keywords elastic-support boundary, pre-twisted beam, semi-analytic method, modal strain energy ratio, torsional vibration

Received August 3, 2019; accepted November 25, 2019

Jin ZENG, Chenguang ZHAO, Hui MA (✉), Bangchun WEN
School of Mechanical Engineering and Automation, Northeastern University, Shenyang 110819, China
E-mails: mahui_2007@163.com; huima@me.neu.edu.cn

Hui MA
Key Laboratory of Vibration and Control of Aero-Propulsion System Ministry of Education, Northeastern University, Shenyang 110819, China

1 Introduction

Rotating pre-twisted beam-like structures are extensively used in machinery; aerospace industry; and power systems [1], such as fan blades [2], marine propellers [3], and wind turbines [4]. The important feature of this kind of structure is that its modal characteristics are closely related to many engineering failure problems such as flutter, stability, and fatigue failure [5,6]. Therefore, many studies have investigated its dynamic characteristics through experimental, analytical, and numerical methods [7–12].

Early studies were primarily focused on the rotating pre-twisted cantilever beam. Adopting Hamilton's principle and Newtonian method, Hodges and Dowell [13] theoretically derived the coupled flapwise–chordwise–axial–torsional equations of motion of a rotating pre-twisted Euler–Bernoulli beam and found that Hamilton's principle was easier and more precise to handle the equations of motion than the Newtonian method due to lesser chance of inadvertently omitting some important terms. Zhu [14] utilized the Rayleigh–Ritz method to establish the coupled flapwise–chordwise–axial equations of motion of a pre-twisted rotating Timoshenko beam and discussed the effects of some parameters (i.e., slenderness ratio, hub radius ratio, and rotational speed) on the natural frequencies of the structure. Ma et al. [15] discussed the effect of the tip shroud rubbing on the coupled flapwise–axial vibration responses of the rotating untwisted Euler–Bernoulli beam. In their later work [16], the effects of the pre-twisted angle, setting angle, and shear deformation were further included. However, the developed model in Ref. [16] was not suitable for simulating the dynamic behaviors of the structure with a larger pre-twisted angle. Sinha [17] utilized the Rayleigh–Ritz method to determine the coupled flapwise–axial–torsional vibration characteristics of a rotating pre-twisted beam suffering from contact load and Coulomb friction. However, the limitation of the proposed model in Ref. [17] was its inability to acquire the classical two-stripe mode of the structure. Yang et al. [18] adopted the power series method to investigate the

dynamic frequencies varying with the rotating speed and setting angles, as well as corresponding complex mode shapes of a rotating tapered and pre-twisted cantilever beam with flapwise–chordwise–axial–torsional coupling. Şakar and Sabuncu [19] used a finite element method to establish the coupled flapwise–chordwise–axial dynamic model of a rotating pre-twisted aerofoil cross-section cantilever Euler–Bernoulli beam. However, both spin softening and Coriolis effects were ignored in Ref. [19]. Based on the same mathematical model in Ref. [19], the effect of shear deformation was further considered by Sabuncu and Evran [20]. They found that the stability of the studied structure increased with decreasing stagger angle and increasing rotational speed and disk radius. Subrahmanyam et al. [21] utilized the Galerkin method in combination with a linear perturbation technique to solve the coupled flapwise–chordwise–torsional equations of motion of a rotating pre-twisted Euler–Bernoulli cantilever beam. The authors claimed that the accuracy of the structure with the second-degree geometric nonlinearities included was adequate and the introduction of nonlinear terms into the thin blades easily resulted in torsional divergence. Discarding the effects of Coriolis and axial inertia, Sina and Haddadpour [22] established the torsional equations of motion of a rotating pre-twisted thin-walled composite beam and indicated that the pre-twisted angle and material anisotropy had remarkable influence on the torsional behaviors of the studied structure, including torsional frequency and hardening/softening effect. Adair and Jaeger [23] ignored the spin softening and Coriolis effects and then applied the modified Adomian decomposition method to obtain the coupled flapwise–chordwise free vibration characteristics of a uniform pre-twisted rotating Euler–Bernoulli beam. The developed model was verified using natural frequency comparisons with the published results, and the influence of the pre-twisted angle and rotating speed on the frequency characteristics was also investigated. Oh and Yoo [24] combined Kane's method with the Galerkin method to establish the coupled flapwise–chordwise–axial–torsional dynamic model of a rotating pre-twisted cantilever beam with arbitrary cross-section. The numerical results indicated that the proposed model had good precision via the comparisons of the modal characteristics obtained from a commercial finite element code. Lee and Lee [25] and Banerjee [26] applied the transfer matrix method to determine the exact flapwise and chordwise modal characteristics of a rotating pre-twisted cantilever beam, and the availability of the proposed models was also verified using natural characteristic comparisons with the literatures. Subrahmanyam and Kaza [27] employed the finite-difference approach and the potential energy method to solve the coupled bending–bending equations of motion of a torsionally rigid slender beam. The results showed that the inclusion of the Coriolis effects was significant for beams with moderate to large thickness ratios and insignificant for beams with small thickness ratios. Hashemi and Richard [28] utilized a dynamic finite element to determine the natural frequencies and mode shapes of rotating assemblages made of beams, which was verified via two illustrative examples of vertical and radial beams with Coriolis effect included. Banerjee and Kennedy [29] used an exact dynamic stiffness method to study the in-plane free vibrations of a rotating beam, which covered the effects of Coriolis force, hub radius, and outboard force. The results revealed that the coupling between bending and axial deformations was rather distinct. Considering the effects of anisotropic material, rotary inertia, and shear deformation, Oh et al. [30] established the coupled bending–bending equations of motion of a rotating pre-twisted box beam, which was verified by means of eigenfrequency characteristics against the results obtained from the literatures. Latalski et al. [31] investigated the coupled bending–shear–twist vibration characteristics of a thin-walled rotating cantilevered beam composed of composite material. In particular, the hub equation resulting from the rotation angle was also included in the structure. The results showed that the maximum magnitude of the flexural–torsional mode coupling for the circumferentially asymmetric stiffness configuration occurred at a ply angle of 74°. Ondra and Titurus [32] established the coupled bending–bending–torsional equations of motion of the rotating pre-twisted beam–tendon system, whose natural frequencies and mode shapes are determined via the combination of a boundary value problem solver and differential quadrature method. In addition, the effects of rotation, pre-twist, and cross-sectional coupling on the modal characteristics of the system were also discussed.

However, in many engineering applications, it is very difficult to enforce the infinite rigidity at the cantilever end of the pre-twisted beam-like structure. In Refs. [33–35], the numerical and experimental results indicated some differences in the low-order modes between a pre-twisted cantilever blade with a tenon and that without a tenon, which also indicated that the root flexibility for the practical cantilevered beam-like structures should be considered. Ignoring the Coriolis effect, the coupled flapwise–chordwise dynamic characteristics of a rotating, in-extensional, and pre-twisted Euler–Bernoulli beam with elastic free boundaries were solved by Lin [36] using the transition matrix method. Based on the developed model, the instability mechanism of the rotating beam was investigated under different parameter influences. In their later works [37,38], a tip mass was added into the preceding model in Ref. [36]. In Ref. [37], the self-adjointness of the structure and the symmetric properties of the matrix Green functions were revealed, and some parameter influences on the natural frequencies of pre-twisted and untwisted beams are discussed in Ref. [38]. Ignoring the Coriolis effect, Choi and Chou [39] applied the modified differential quadrature method to solve the coupled flapwise–chordwise free vibration of a rotating,

in-extensional, and pre-twisted Timoshenko beam with elastic–elastic boundaries. The advantages of the proposed method were the permission of any combinations of end restraining conditions. Bambill et al. [40] utilized the differential quadrature method in combination with the domain decomposition to analyze the flapwise vibration behaviors of a rotating tapered multi-span beam under the effect of spring stiffness. The results showed that the translational spring stiffness had more significant effects on the dynamic characteristics of the structure than the rotational spring stiffness. Digilov and Abramovich [41] conducted theoretical and experimental studies of the impact of root flexibility on the flapwise vibration of a uniform beam where the shear deformation and rotary inertia were left out.

According to the literatures listed above, most were conducted on the free vibrations of the rotating pre-twisted beam with clamped boundary conditions, whose torsional vibration are ignored in most cases. In addition, the centrifugal stiffening effect in the torsional direction and Coriolis effect were overlooked in many literatures. In particular, the introduction of non-zero setting angle, pre-twisted angle, and rotating speed can result in vibration coupling among the flapwise, chordwise, and torsional directions, but quantitative studies on the corresponding degree of coupling are limited. Considering these deficiencies, the present study established a dynamic model of the rotating inclined beams with twisted-shape sections and elastically restrained root using Hamilton's principle in combination with the assumed mode method. Numerical simulation in ANSYS and experimental test were conducted to verify the proposed model. Next, the modal strain energy ratio (MSER) affected by the setting angle, pre-twisted angle, and rotating speed was utilized to quantify the degree of coupling among flapwise, chordwise, and torsional directions. Finally, some conclusions were made.

2 Mathematical modeling

2.1 Establishment of kinetic and potential energies

In engineering applications, it is difficult to apply the infinite rigidity to the beam root, thereby leading to the existence of certain flexibilities. On this basis, the schematic of a pre-twisted and double-tapered beam with elastic supports is shown in Fig. 1. In Fig. 1, $OXYZ$, $O^rX^rY^rZ^r$, $o^dx^dy^dz^d$, and $oxyz$ are the global coordinate system, the rotating coordinate system, the local coordinate system attached to the joint surface on the disk, and the local coordinate system attached to the arbitrary beam section, respectively; β_0 and $\gamma(L)$ are the initial setting and pre-twisted angles, respectively (see Fig. 1(b)); three linear (u, v, w) and three angular (θ, ϕ, ψ) displacement components of o in $oxyz$ are assumed (see Fig. 1(c)). Accordingly, three linear (k_x, k_y, k_z) and three angular (k_{rx}, k_{ry}, k_{rz}) supporting stiffness are established to simulate the flexibility of the root section of the beam, as shown in Fig. 1(a).

In Fig. 1(b), the setting angle β of an arbitrary beam section can be calculated based on the linear interpolation hypothesis:

$$\beta = \beta_0 + \gamma, \tag{1}$$

where $\gamma = \gamma(L)x/L$ is the pre-twisted angle at the initial coordinate x in $o^dx^dy^dz^d$ and L is the beam length.

Combining Fig. 1(a) with Fig. 1(c), the coordinates of an arbitrary point "p" on the beam section in $OXYZ$ can be expressed as follows:

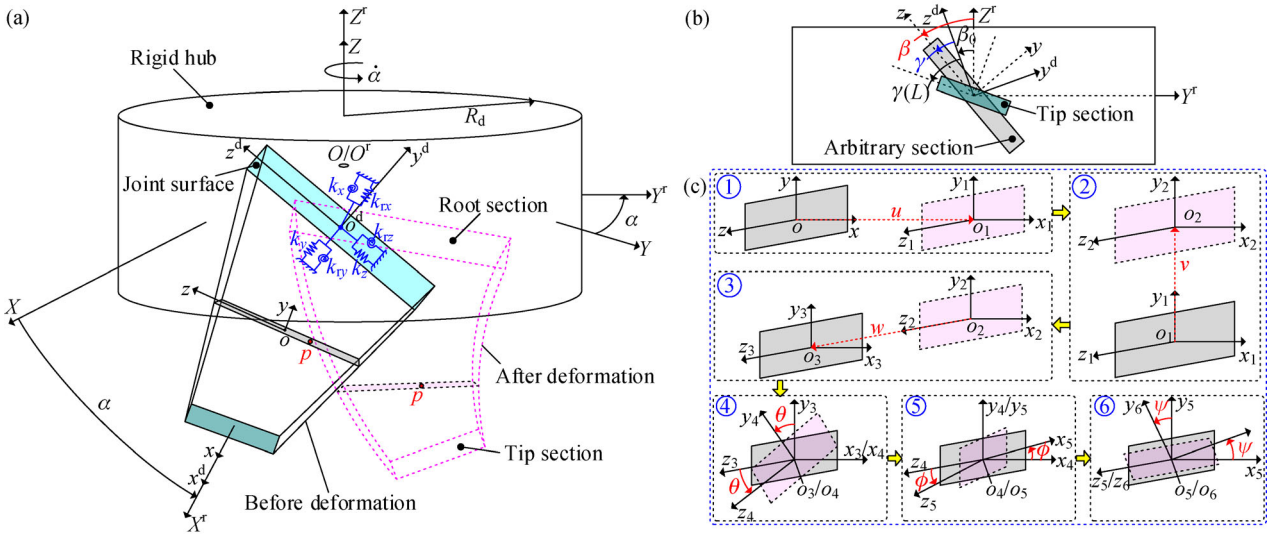

Fig. 1 Pre-twisted and double-tapered beam: (a) Reference frames, (b) pre-twisted and setting angles, and (c) deformation modes of an arbitrary section.

$$\boldsymbol{r}_p = \begin{bmatrix} X_p \\ Y_p \\ Z_p \end{bmatrix} = \boldsymbol{A}_5\boldsymbol{A}_4\left(\begin{bmatrix} R_\mathrm{d}+x+u \\ v \\ w \end{bmatrix} + \boldsymbol{A}_3\boldsymbol{A}_2\boldsymbol{A}_1\begin{pmatrix} 0 \\ y \\ z \end{pmatrix}\right), \tag{2}$$

where R_d is the disk radius, y and z are the coordinates of p in oyz, and $\boldsymbol{A}_1$, $\boldsymbol{A}_2$, $\boldsymbol{A}_3$, $\boldsymbol{A}_4$, and $\boldsymbol{A}_5$ are a series of transformation matrices from $oxyz$ to $OXYZ$, whose expressions are shown as follows:

$$\boldsymbol{A}_1 = \begin{bmatrix} 1 & -\psi & 0 \\ \psi & 1 & 0 \\ 0 & 0 & 1 \end{bmatrix},\ \boldsymbol{A}_2 = \begin{bmatrix} 1 & 0 & \varphi \\ 0 & 1 & 0 \\ -\varphi & 0 & 1 \end{bmatrix},$$

$$\boldsymbol{A}_3 = \begin{bmatrix} 1 & 0 & 0 \\ 0 & 1 & -\theta \\ 0 & \theta & 1 \end{bmatrix},\ \boldsymbol{A}_4 = \begin{bmatrix} 1 & 0 & 0 \\ 0 & \cos\beta & -\sin\beta \\ 0 & \sin\beta & \cos\beta \end{bmatrix},$$

$$\boldsymbol{A}_5 = \begin{bmatrix} \cos\alpha & -\sin\alpha & 0 \\ \sin\alpha & \cos\alpha & 0 \\ 0 & 0 & 1 \end{bmatrix}. \tag{3}$$

Here, the small deformation in this work is assumed, and only first-order Taylor expansion is adopted in Eq. (3).

To make the mode shapes of the uniform straight link/beam applicable to discretize the equations of motion of the pre-twisted beam, some necessary displacement transformations are needed first. In this work, the displacements $\boldsymbol{q} = [u, v, w, \theta, \phi, \psi]^\mathrm{T}$ in $oxyz$ are represented by the displacement $\boldsymbol{Q} = [U, V, W, \Theta, \Phi, \Psi]^\mathrm{T}$ in $o^\mathrm{d}x^\mathrm{d}y^\mathrm{d}z^\mathrm{d}$.

$$\boldsymbol{q} = \begin{bmatrix} 1 & 0 & 0 & 0 & 0 & 0 \\ 0 & \cos\gamma & \sin\gamma & 0 & 0 & 0 \\ 0 & -\sin\gamma & \cos\gamma & 0 & 0 & 0 \\ 0 & 0 & 0 & 1 & 0 & 0 \\ 0 & 0 & 0 & 0 & \cos\gamma & \sin\gamma \\ 0 & 0 & 0 & 0 & -\sin\gamma & \cos\gamma \end{bmatrix}\boldsymbol{Q}. \tag{4}$$

Substituting Eqs. (3) and (4) into Eq. (2) the kinetic energy T_b of the rotating, pre-twisted, double-tapered, and elastic-supported beam can be calculated as follows:

$$T_\mathrm{b} = \frac{1}{2}\rho\int_0^L \mathrm{d}x \iint_A \dot{\boldsymbol{r}}_p^\mathrm{T}\dot{\boldsymbol{r}}_p \mathrm{d}y\mathrm{d}z, \tag{5}$$

where an over-dot represents the differentiation with respect to time t, ρ is the density, and A is the sectional area at x in $o^\mathrm{d}x^\mathrm{d}y^\mathrm{d}z^\mathrm{d}$ (see Fig. 1(a)).

The corresponding potential energy U_b is given as follows:

$$\begin{aligned} U_\mathrm{b} = {} & \frac{1}{2}E\int_0^L \left[AU'^2 + (I_z\cos^2\gamma + I_y\sin^2\gamma)\Psi'^2 + (I_y - I_z)\sin(2\gamma)\Psi'\Phi' + (I_z\sin^2\gamma + I_y\cos^2\gamma)\Phi'^2 + \frac{GJ}{E}\Theta'^2\right]\mathrm{d}x \\ & + \frac{1}{2}\rho\dot{\alpha}^2\int_0^L A(R_\mathrm{d}+x)\left[\int_0^x \left(W'^2 + V'^2 + \widehat{\frac{I_x}{A}\Theta'^2}\right)\mathrm{d}x\right]\mathrm{d}x + \frac{1}{2}G\int_0^L \kappa_y A(V' - \Psi)^2\mathrm{d}x + \frac{1}{2}G\int_0^L \kappa_z A(W' + \Phi)^2\mathrm{d}x \\ & + \frac{1}{2}k_x U^2|_{x=0} + \frac{1}{2}k_y V^2|_{x=0} + \frac{1}{2}k_z W^2|_{x=0} + \frac{1}{2}k_{\mathrm{r}x}\Theta^2|_{x=0} + \frac{1}{2}k_{\mathrm{r}y}\Phi^2|_{x=0} + \frac{1}{2}k_{\mathrm{r}z}\Psi^2|_{x=0}, \end{aligned} \tag{6}$$

where E and G are Young's modulus and shear modulus, respectively, $I_y = hb^3/12$ and $I_z = bh^3/12$ are the second moments of area in the y- and z-axes at x in $o^\mathrm{d}x^\mathrm{d}y^\mathrm{d}z^\mathrm{d}$, respectively, $b = (1-\tau_\mathrm{b}x/L)b_0$ and $h = (1-\tau_\mathrm{h}x/L)h_0$ are the width and thickness of the beam section located at x in $o^\mathrm{d}x^\mathrm{d}y^\mathrm{d}z^\mathrm{d}$, b_0 and h_0 are the width and thickness of the root section (see Fig. 1(a)), respectively, τ_b and τ_h are the tapered ratios of the width and thickness, respectively; $A = bh$ is the area of the beam section at x in $o^\mathrm{d}x^\mathrm{d}y^\mathrm{d}z^\mathrm{d}$, and κ_y and κ_z are the shear coefficients in the y- and z-directions, respectively. In Eq. (6), $\widehat{(\cdot)}$ are the terms related to centrifugal stiffening effect in torsional vibration [42].

In Eq. (6), J is the torsional moment of inertia, and the corresponding computational formula is written as follows [43]:

$$J = J_\mathrm{s} + J_a,\ J_\mathrm{s} = \left[\frac{1}{3} - \frac{64h}{\pi^5 b}\tanh\left(\frac{\pi b}{2h}\right)\right]bh^3,$$

$$J_a = \frac{E\gamma(L)^2}{720GL^2}[bh(9b^4 + 10b^2h^2 + 9h^4) - 60I_x(b^2+h^2)], \tag{7}$$

where b and h are the width and thickness of an arbitrary rectangular beam section, respectively, and $I_x = I_y + I_z$ is the polar moment of inertia.

2.2 Galerkin discretization

Applying Hamilton's principle to Eqs. (5) and (6), six partial differential equations of motion can be then determined as follows:

Partial differential equations of motion in the x^{d}-direction:

$$\left\{\begin{array}{l}\int_0^L \rho A\ddot{U}\delta U\mathrm{d}x-\int_0^L \rho A\dot{\alpha}^2 U\delta U\mathrm{d}x\\ -2\int_0^L \rho A\dot{\alpha}\cos\beta_0\dot{V}\delta U\mathrm{d}x+2\int_0^L \rho A\sin\beta_0\dot{\alpha}\dot{W}\delta U\mathrm{d}x\\ -\int_0^L \rho A\ddot{\alpha}\cos\beta_0 V\delta U\mathrm{d}x+\int_0^L \rho A\ddot{\alpha}\sin\beta_0 W\delta U\mathrm{d}x\\ +E\int_0^L AU'\delta U'\mathrm{d}x-\int_0^L \rho A(R_{\mathrm{d}}+x)\dot{\alpha}^2\delta U\mathrm{d}x+k_x U\delta U|_{x=0}\end{array}\right\}=0. \tag{8}$$

Partial differential equations of motion in the y^{d}-direction:

$$\left\{\begin{array}{l}\int_0^L \rho A\ddot{V}\delta V\mathrm{d}x-\int_0^L \rho A\dot{\alpha}^2\cos^2\beta_0 V\delta V\mathrm{d}x\\ +\int_0^L \rho A\ddot{\alpha}\cos\beta_0 U\delta V\mathrm{d}x\\ +0.5\int_0^L \rho A\dot{\alpha}^2\sin(2\beta_0)W\delta V\mathrm{d}x\\ +2\int_0^L \rho A\dot{\alpha}\cos\beta_0\dot{U}\delta V\mathrm{d}x\\ +\int_0^L \rho A\ddot{\alpha}\cos\beta_0(R_{\mathrm{d}}+x)\delta V\mathrm{d}x\\ +\rho\dot{\alpha}^2\int_0^L (R_{\mathrm{d}}+x)A\left(\int_0^x V'\delta V'\mathrm{d}x\right)\mathrm{d}x\\ +\kappa_y G\int_0^L A(V'-\Psi)\delta V'\mathrm{d}x+k_y V\delta V|_{x=0}\end{array}\right\}=0. \tag{9}$$

Partial differential equations of motion in the z^{d}-direction:

$$\left\{\begin{array}{l}\int_0^L \rho A\ddot{W}\delta W\mathrm{d}x-\int_0^L \rho A\dot{\alpha}^2\sin^2\beta_0 W\delta W\mathrm{d}x\\ -\int_0^L \rho A\ddot{\alpha}\sin\beta_0 U\delta W\mathrm{d}x+0.5\int_0^L \rho A\dot{\alpha}^2\sin(2\beta_0)V\delta W\mathrm{d}x\\ -2\int_0^L \rho A\dot{\alpha}\sin\beta_0\dot{U}\delta W\mathrm{d}x-\int_0^L \rho A\ddot{\alpha}(R_{\mathrm{d}}+x)\sin\beta_0\delta W\mathrm{d}x\\ +\int_0^L \rho\dot{\alpha}^2 A(R_{\mathrm{d}}+x)\left(\int_0^x W'\delta W'\mathrm{d}x\right)\mathrm{d}x\\ +k_z G\int_0^L A(W'+\Phi)\delta W'\mathrm{d}x+k_z W\delta W|_{x=0}\end{array}\right\}=0. \tag{10}$$

Partial differential equations of motion in the rotx^{d}-direction:

$$\left\{\begin{array}{l}\int_0^L \rho(I_z+I_y)\ddot{\Theta}\delta\Theta\mathrm{d}x-\int_0^L \rho\dot{\alpha}^2(I_y\cos^2\beta+I_z\sin^2\beta)\Theta\delta\Theta\mathrm{d}x\\ -2\int_0^L \rho\dot{\alpha}(I_y\cos\gamma\cos\beta+I_z\sin\gamma\sin\beta)\dot{\Phi}\delta\Theta\mathrm{d}x\\ -2\int_0^L \rho\dot{\alpha}(I_y\cos\beta\sin\gamma-I_z\cos\gamma\sin\beta)\dot{\Psi}\delta\Theta\mathrm{d}x\\ -\int_0^L \rho\ddot{\alpha}(I_z\sin\gamma\sin\beta+I_y\cos\gamma\sin\beta)\Theta\delta\Theta\mathrm{d}x\\ +\int_0^L \rho\ddot{\alpha}(I_z\cos\gamma\sin\beta-I_y\sin\gamma\cos\beta)\Psi\delta\Theta\mathrm{d}x\\ +0.5\int_0^L \rho\dot{\alpha}^2\left(I_z-I_y\right)\sin(2\beta)\delta\Theta\mathrm{d}x+G\int_0^L J\Theta'\delta\Theta'\mathrm{d}x\\ +\rho\dot{\alpha}^2\int_0^L (R_{\mathrm{d}}+x)A\left(\int_0^x\frac{I_x}{A}\Theta'\delta\Theta'\mathrm{d}x\right)\mathrm{d}x+k_{\mathrm{r}x}\Theta\delta\Theta|_{x=0}\end{array}\right\}=0. \tag{11}$$

Partial differential equations of motion in the roty$^{\mathrm{d}}$-direction:

$$\left\{\begin{array}{l}\int_0^L \rho(I_y\cos^2\gamma+I_z\sin^2\gamma)\ddot{\Theta}\delta\Theta\mathrm{d}x\\ -\int_0^L \rho\dot{\alpha}^2(I_y\cos^2\gamma+I_z\sin^2\gamma)\Phi\delta\Phi\mathrm{d}x\\ +2\int_0^L \rho\dot{\alpha}(I_y\cos\gamma\cos\beta+I_z\sin\gamma\sin\beta)\dot{\Theta}\delta\Theta\mathrm{d}x\\ +\int_0^L \rho\ddot{\alpha}(I_y\cos\gamma\cos\beta+I_z\sin\gamma\sin\beta)\Theta\delta\Phi\mathrm{d}x\\ +0.5\int_0^L \rho(I_y-I_z)\sin(2\gamma)\ddot{\Psi}\delta\Phi\mathrm{d}x\\ +\int_0^L \rho[I_y\cos\gamma\sin\beta-I_z\sin\gamma\cos\beta]\ddot{\alpha}\delta\Phi\mathrm{d}x\\ +0.5E\int_0^L (I_y-I_z)\sin(2\gamma)\Psi'\delta\Phi'\mathrm{d}x\\ +0.5\int_0^L \rho\dot{\alpha}^2(I_z-I_y)\sin(2\gamma)\Psi\delta\Phi\mathrm{d}x\\ +E\int_0^L (I_y\cos^2\gamma+I_z\sin^2\gamma)\Phi'\delta\Phi'\mathrm{d}x\\ +\kappa_z G\int_0^L A(W'+\Phi)\delta\Phi\mathrm{d}x+k_{\mathrm{r}y}\Phi\delta\Phi|_{x=0}\end{array}\right\}=0 \tag{12}$$

Partial differential equations of motion in the rotz$^{\mathrm{d}}$-direction:

$$\left\{\begin{array}{l}\int_0^L\rho(I_z\cos^2\gamma+I_y\sin^2\gamma)\ddot{\Psi}\delta\Psi\mathrm{d}x\\ -\int_0^L\rho\dot{\alpha}^2(I_z\cos^2\gamma+I_y\sin^2\gamma)\Psi\delta\Psi\mathrm{d}x\\ +2\int_0^L\rho\dot{\alpha}(I_y\sin\gamma\cos\beta-I_z\cos\gamma\sin\beta)\dot{\Theta}\delta\Psi\mathrm{d}x\\ +\int_0^L\rho\ddot{\alpha}(I_y\sin\gamma\cos\beta-I_z\cos\gamma\sin\beta)\Theta\delta\Psi\mathrm{d}x\\ +0.5\int_0^L\rho\Big(I_y-I_z\Big)\sin(2\gamma)\ddot{\Phi}\delta\Psi\mathrm{d}x\\ +\frac{1}{2}E\int_0^L\Big(I_y-I_z\Big)\sin(2\gamma)\Phi'\delta\Psi'\mathrm{d}x\\ -0.5\int_0^L\rho\dot{\alpha}^2\Big(I_y-I_z\Big)\sin(2\gamma)\Phi\delta\Psi\mathrm{d}x\\ +\int_0^L\rho\ddot{\alpha}(I_y\sin\gamma\sin\beta+I_z\cos\gamma\cos\beta)\delta\Psi\mathrm{d}x\\ +E\int_0^L(I_z\cos^2\gamma+I_y\sin^2\gamma)\Psi'\delta\Psi'\mathrm{d}x\\ -\kappa_yG\int_0^LA(V'+\Psi)\delta\Psi\mathrm{d}x+k_{\mathrm{rz}}\Psi\delta\Psi|_{x=0}\end{array}\right\}=0 \quad (13)$$

The assumed mode method is utilized to discretize Eqs. (8)–(13) with the first N modes. By introducing canonical coordinates $U_i(t)$, $V_i(t)$, $W_i(t)$, $\Theta_i(t)$, $\Phi_i(t)$, and $\Psi_i(t)$, the displacements U, V, W, Θ, Φ, and Ψ can be expressed as follows:

$$U=\sum_{i=1}^{N}\phi_{1i}(x)U_i(t),\ V=\sum_{i=1}^{N}\phi_{2i}(x)V_i(t),$$

$$W=\sum_{i=1}^{N}\phi_{3i}(x)W_i(t),\ \Theta=\sum_{i=1}^{N}\phi_{4i}(x)\Theta_i(t),$$

$$\Phi=\sum_{i=1}^{N}\phi_{5i}(x)\Phi_i(t),\ \Psi=\sum_{i=1}^{N}\varphi_{6i}(x)\Psi_i(t), \quad (14)$$

where $\Phi_{ji}(x)$ (j = 1, 2, …, 6; i = 1, 2, …, N) is the ith mode shape in the axial, flapwise, chordwise, and torsional rotation in the x- and y-axes and rotation in the z-axis. The corresponding expressions are as follows:

$$\left\{\begin{array}{l}\phi_{1i}=\cos[\beta_{\mathrm{a}i}(L-x)],\\ \phi_{2i}=\cosh[\beta_{\mathrm{f}i}(L-x)]+\cos[\beta_{\mathrm{f}i}(L-x)]+\xi_{\mathrm{f}i}\{\sinh[\beta_{\mathrm{f}i}(L-x)]+\sin[\beta_{\mathrm{f}i}(L-x)]\},\\ \phi_{3i}=\cosh[\beta_{\mathrm{c}i}(L-x)]+\cos[\beta_{\mathrm{c}i}(L-x)]+\xi_{\mathrm{c}i}\{\sinh[\beta_{\mathrm{c}i}(L-x)]+\sin[\beta_{\mathrm{c}i}(L-x)]\},\\ \phi_{4i}=\cos[\beta_{\mathrm{t}i}(L-x)],\\ \phi_{5i}=\dfrac{\phi'_{3i}}{i\pi},\\ \phi_{6i}=\dfrac{\phi'_{2i}}{i\pi},\end{array}\right. \quad (15)$$

where $\beta_{\mathrm{a}i}$, $\beta_{\mathrm{f}i}$, $\beta_{\mathrm{c}i}$, and $\beta_{\mathrm{t}i}$ are the ith (i = 1, 2, …, N) roots of the characteristic equations in Eqs. (16a)–(16d).

$$\beta_{\mathrm{a}}L\tan(\beta_{\mathrm{a}}L)=\frac{k_xL}{EA|_{x=0}}, \quad (16a)$$

$$\left\{\begin{array}{l}E^2I_z^2(\beta_{\mathrm{f}}L)^4[1-\cosh(\beta_{\mathrm{f}}L)\cos(\beta_{\mathrm{f}}L)]\\ -EI_z(\beta_{\mathrm{f}}L)^3Lk_{\mathrm{rz}}[\cosh(\beta_{\mathrm{f}}L)\sin(\beta_{\mathrm{f}}L)+\sinh(\beta_{\mathrm{f}}L)\cos(\beta_{\mathrm{f}}L)]\\ +EI_z(\beta_{\mathrm{f}}L)L^3k_y[\sinh(\beta_{\mathrm{f}}L)\cos(\beta_{\mathrm{f}}L)-\cosh(\beta_{\mathrm{f}}L)\sin(\beta_{\mathrm{f}}L)]\\ +k_yk_{\mathrm{rz}}L^4[1+\cosh(\beta_{\mathrm{f}}L)\cos(\beta_{\mathrm{f}}L)]\end{array}\right\}=0, \quad (16b)$$

$$\left\{\begin{array}{l}E^2I_y^2(\beta_{\mathrm{c}}L)^4[1-\cosh(\beta_{\mathrm{c}}L)\cos(\beta_{\mathrm{c}}L)]\\ -EI_z(\beta_{\mathrm{c}}L)^3Lk_{\mathrm{ry}}[\cosh(\beta_{\mathrm{c}}L)\sin(\beta_{\mathrm{c}}L)+\sinh(\beta_{\mathrm{c}}L)\cos(\beta_{\mathrm{c}}L)]\\ +EI_y(\beta_{\mathrm{c}}L)L^3k_z[\sinh(\beta_{\mathrm{c}}L)\cos(\beta_{\mathrm{c}}L)-\cosh(\beta_{\mathrm{c}}L)\sin(\beta_{\mathrm{c}}L)]\\ +k_zk_{\mathrm{ry}}L^4[1+\cosh(\beta_{\mathrm{c}}L)\cos(\beta_{\mathrm{c}}L)]\end{array}\right\}=0, \quad (16c)$$

$$\beta_{\mathrm{t}}L\tan(\beta_{\mathrm{t}}L)=\frac{k_{\mathrm{r}x}L}{GJ}. \quad (16d)$$

In addition, the coefficients $\xi_{\mathrm{f}i}$ and $\xi_{\mathrm{c}i}$ in Eq. (15) can be calculated using the two following formulas:

$$\xi_{\mathrm{f}i}=-\frac{EI_z\beta_{\mathrm{f}i}[\cosh(\beta_{\mathrm{f}i}L)-\cos(\beta_{\mathrm{f}i}L)]+k_{\mathrm{rz}}[\sinh(\beta_{\mathrm{f}i}L)-\sin(\beta_{\mathrm{f}i}L)]}{EI_z\beta_{\mathrm{f}i}[\sin(\beta_{\mathrm{f}i}L)-\sin(\beta_{\mathrm{f}i}L)]+k_{\mathrm{rz}}[\cosh(\beta_{\mathrm{f}i}L)+\cos(\beta_{\mathrm{f}i}L)]}, \quad (17a)$$

$$\xi_{ci} = -\frac{EI_y\beta_{ci}[\cosh(\beta_{ci}L)-\cos(\beta_{ci}L)]+k_{ry}[\sinh(\beta_{ci}L)-\sin(\beta_{ci}L)]}{EI_y\beta_{ci}[\sin(\beta_{ci}L)-\sin(\beta_{ci}L)]+k_{ry}[\cosh(\beta_{ci}L)+\cos(\beta_{ci}L)]}. \quad (17b)$$

Substituting Eqs. (14), (15), and (17) into Eqs. (8)–(13), the equations of motion of the model can be expressed as follows:

$$\boldsymbol{M}\ddot{\boldsymbol{q}} + \boldsymbol{C}\dot{\boldsymbol{q}} + (\boldsymbol{K}_e + \boldsymbol{K}_c + \boldsymbol{K}_s + \boldsymbol{K}_{acc})\boldsymbol{q} = \boldsymbol{F}, \quad (18)$$

where $\boldsymbol{M}$, $\boldsymbol{C}$, $\boldsymbol{K}_e$, $\boldsymbol{K}_c$, $\boldsymbol{K}_s$, and $\boldsymbol{K}_{acc}$ are mass, Coriolis force, structural stiffness, centrifugal stiffening, spin softening, and angular acceleration-induced stiffness matrices, respectively, and $\boldsymbol{q}$ and $\boldsymbol{F}$ are canonical coordinates and external force vector, respectively.

2.3 Model verification

In this section, the supporting stiffness of the proposed model (i.e., k_x, k_y, k_z, k_{rx}, k_{ry}, k_{rz}) is first calibrated via the experimental tests in combination with the genetic algorithm embedded in MATLAB toolbox. Then, the dynamic frequency characteristics of the calibrated semi-analytical model are verified based on the results obtained from the ANSYS models. Here, the specimen is made out of 2A12-T4 aluminum alloy. The corresponding material and geometrical parameter settings are listed as below:

Material properties: Young's modulus E = 71.7 GPa; Density ρ = 2770 kg/m^3; and Poisson's ratio v = 0.33.

Geometrical properties: Beam length L = 160 mm; Beam root width b_0= 25.2 mm; Beam root thickness h_0= 4.2 mm; Disk radius R_d = 150 mm; Tapered ratio of thickness τ_h = 0.4048; Tapered ratio of width τ_b = 0.3056; and Shear factors $\kappa_y = \kappa_z$ = 5/6.

2.3.1 Calibration experiment on supporting stiffness

Before calibrating the elastic supporting stiffness, hammering and sweep-frequency tests are first conducted, as shown in Fig. 2. In the hammering test, additional testing instruments such as a force-hammer (PCB086C01) and a laser vibrometer (Polytec PDV-10) are adopted (see Fig. 2(a)). In the sweep-frequency test, a piezoelectric accelerometer (CA-YD-125, 1.5 g) and a shaker table (EDM-5000, 5–2500 Hz) are utilized (see Fig. 2(b)). Figure 2(c) shows the LMS front controller of a data acquisition system.

Based on the test system shown in Fig. 2, the first three-order natural frequencies of the tested specimen under $\beta(L)$ = 45° are 164.3, 578.5, and 1149 Hz for the hammering test (see Fig. 3(a)) and 165, 580.5, and 1150 Hz for the frequency-sweep test (see Fig. 3(b)). Specifically, the three sections of frequency sweep are adopted in the sweep-frequency test for the sake of reducing the frequency-sweep time and exciting the first three-order natural frequencies as far as possible (see Figs. 2(b) and 3(b)). As a whole, the results obtained from both tests agree well with each other. In particular, the first three-order natural frequencies obtained from the hammering test are utilized to establish the optimized objective function Z shown in Eq. (19).

$$Z = \sqrt{\left(f_{n1}(\boldsymbol{k})-164.3\right)^2+\left(f_{n2}(\boldsymbol{k})-578.5\right)^2+\left(f_{n3}(\boldsymbol{k})-1149\right)^2}, \quad (19)$$

where f_{ni} (i = 1, 2, 3) is the state variables, and $\boldsymbol{k}$ = [k_x, k_y, k_z, k_{rx}, k_{ry}, k_{rz}] is a vector related to the six design variables. Considering that the beam is clamped free, the supporting stiffness should be not too small. On this basis, the variation range of the supporting stiffness is all pre-supposed as [1 × 10^6, 2 × 10^8], and then the genetic algorithm is adopted to find the optimal stiffness combinations minimizing Z. The flow chart of the genetic algorithm adopted is shown in Fig. 4. In this work, the optimal k_x, k_y, k_z, k_{rx}, k_{ry}, and k_{rz} are finally determined as follows: k_x = 7.26 × 10^6 N/m, k_y = 1.4 × 10^6 N/m, k_z = 2 × 10^7 N/m, k_{rx} = 3.7 × 10^6 N·m/rad, k_{ry} = 3.8 × 10^6 N·m/rad, and k_{rz} = 2.5 × 10^6 N·m/rad. The first six characteristic roots (see Eqs. (16a)–(17b)) related to the optimal supporting stiffness are listed in as below:

Support stiffness:

k_x = 7.26 ×10^6 N/m;
k_y = 1.4 ×10^6 N/m;
k_z = 2 ×10^7 N/m;
k_{rx}= 3.7×10^6 N·m/rad;
k_{ry} = 3.8 ×10^6 N·m/rad;
k_{rz} = 2.5 ×10^6 N·m/rad.

Characteristic root:

$\boldsymbol{\beta}_a$=[0.3815, 3.1895, 6.3074, 9.4410, 12.5785, 15.7177];
$\boldsymbol{\beta}_f$=[1.8681, 4.4769, 6.8342, 9.1140, 11.9561, 15.0046];
$\boldsymbol{\beta}_c$=[1.8565, 4.1662, 6.1601, 8.8109, 11.8429, 14.9494];
$\boldsymbol{\beta}_t$=[1.5708, 4.7123, 7.8538, 10.9953, 14.1368, 17.2783];
$\boldsymbol{\xi}_c$=[−0.7226, −1.0427, −0.9963, −1.001, −1, −1];
$\boldsymbol{\xi}_f$=[−0.7295, −1.0273, −0.9970, −1.001, −1, −1].

In Table 1, the results obtained from the proposed model with elastic and fixed supports are compared with those obtained from the experimental tests. As shown in Table 1, the results, especially for the higher-order modes under elastic-support boundary, are closer to the experimental results than those under fixed support boundary, which also indicates the impracticability of applying the infinite rigidity to the cantilevered end of the pre-twisted beam based on the fixture shown in Figs. 2(a) and 2(b).

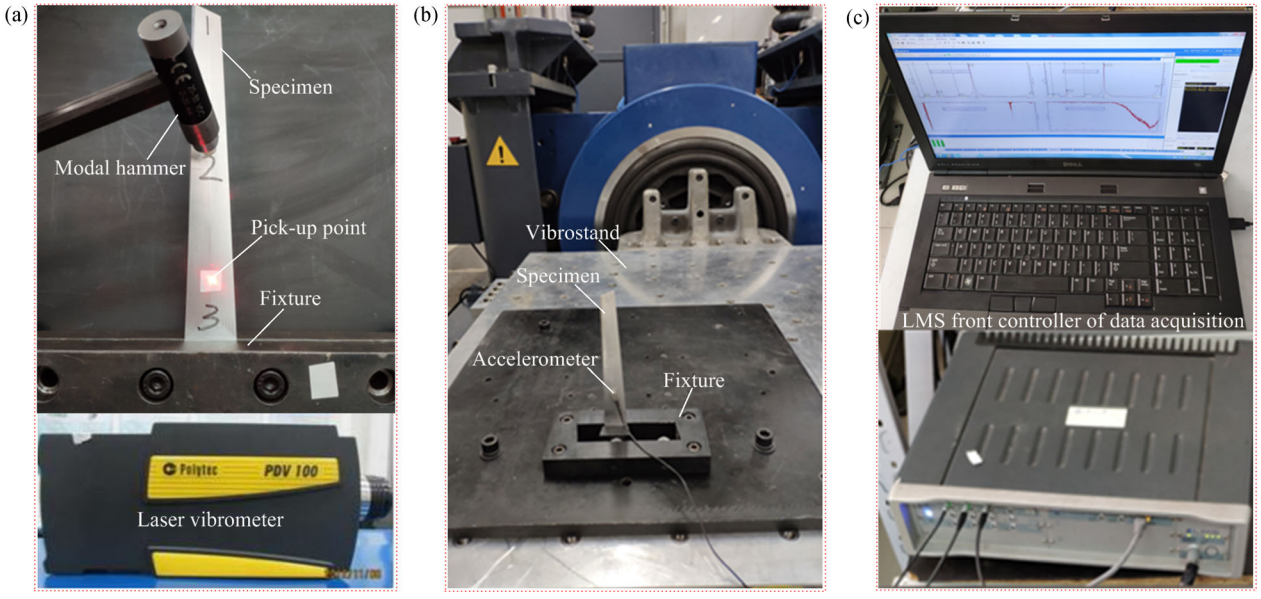

Fig. 2 Test rig: (a) Hammer test, (b) sweep test, and (c) data acquisition system.

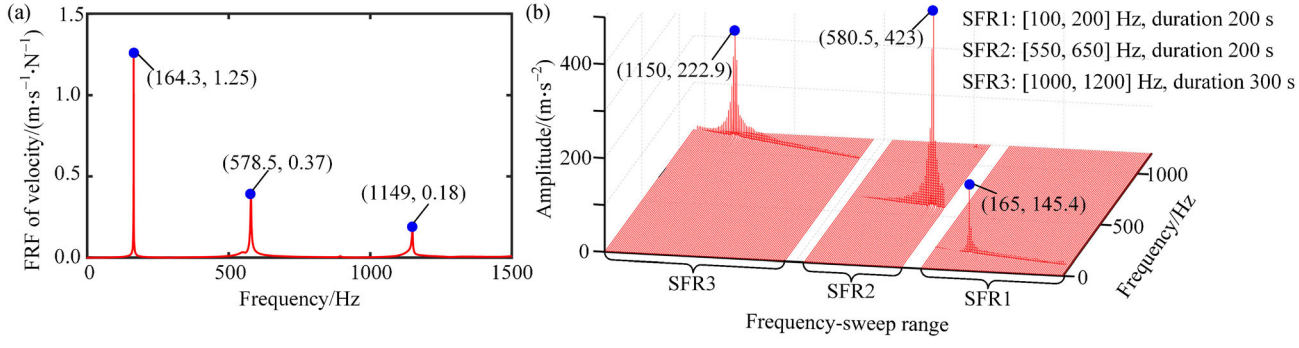

Fig. 3 Experimental results under $\gamma(L) = 45°$: (a) Frequency response function (FRF) of velocity obtained from hammering test and (b) spectrum cascades obtained from the sweep-frequency test. SFR: Sweep-frequency range; 1, 2, and 3: The first, the second, and the third sections of frequency sweep, respectively.

2.3.2 ANSYS verification

In Subsection 2.3.1, the natural characteristics obtained from the proposed model under rotating speed $n = 0$ r/min are calibrated based on the experiments. Here, the corresponding dynamic characteristics are verified against the results obtained in the ANSYS models. In this work, Beam188, Shell181, Matrix27, and Mass21 elements in ANSYS software are adopted to build the finite element model of the pre-twisted beam with elastic supports, as shown in Fig. 5. Here, the elastic supports are simulated via the Matrix27 element, and the corresponding matrix formulation is asymmetric. All the displacement components $\boldsymbol{Q} = [U, V, W, \Theta, \Phi, \Psi]^{\mathrm{T}}$ of the semi-analytical model are determined in $o^{\mathrm{d}}x^{\mathrm{d}}y^{\mathrm{d}}z^{\mathrm{d}}$, and the supporting stiffness k_x, k_y, k_z, k_{rx}, k_{ry}, and k_{rz} in the semi-analytical model are also defined in $o^{\mathrm{d}}x^{\mathrm{d}}y^{\mathrm{d}}z^{\mathrm{d}}$, whereas the finite element model is established in $O^{\mathrm{r}}X^{\mathrm{r}}Y^{\mathrm{r}}Z^{\mathrm{r}}$. Therefore, to make the semi-analytical model and the semi-analytical model equivalent, some necessary stiffness matrix transformation from $o^{\mathrm{d}}x^{\mathrm{d}}y^{\mathrm{d}}z^{\mathrm{d}}$ to $OX^{\mathrm{r}}Y^{\mathrm{r}}Z^{\mathrm{r}}$ is needed and presented as follows:

$$\boldsymbol{K}_{\mathrm{Sup},O^{\mathrm{r}}X^{\mathrm{r}}Y^{\mathrm{r}}Z^{\mathrm{r}}} = \boldsymbol{T}_1^{\mathrm{T}} \begin{bmatrix} k_x & 0 & 0 & 0 & 0 & 0 \\ 0 & k_y & 0 & 0 & 0 & 0 \\ 0 & 0 & k_z & 0 & 0 & 0 \\ 0 & 0 & 0 & k_{\mathrm{rx}} & 0 & 0 \\ 0 & 0 & 0 & 0 & k_{\mathrm{ry}} & 0 \\ 0 & 0 & 0 & 0 & 0 & k_{\mathrm{rz}} \end{bmatrix} \boldsymbol{T}_1,$$

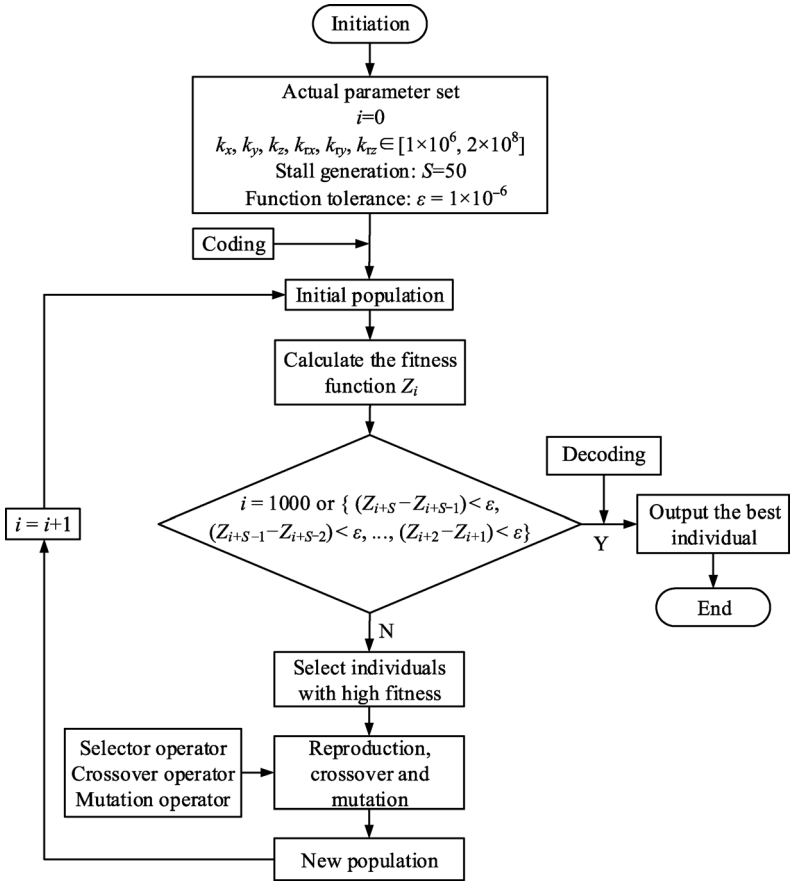

Fig. 4 Flow chart of the genetic algorithm.

Table 1 First three-order natural frequency obtained from the proposed model and experiment

Mode	Frequencies obtained from hammering test (benchmark)/Hz	Frequencies obtained from sweep-frequency test/Hz	Frequencies obtained from proposed model/Hz	
			Fixed support	Elastic support
f_{n1}	164.3	165.0 (0.426%)	160.4 (−2.374%)	159.6 (−2.861%)
f_{n2}	578.5	580.5 (0.346%)	598.2 (3.405%)	580.9 (0.415%)
f_{n3}	1149.0	1150.0 (0.087%)	1208.6 (5.187%)	1149.8 (0.070%)

Note: The values in the brackets are errors relative to the results obtained from the hammering test.

$$\boldsymbol{T}_1 = \begin{bmatrix} 1 & 0 & 0 & 0 & 0 & 0 \\ 0 & \cos\beta_0 & \sin\beta_0 & 0 & 0 & 0 \\ 0 & -\sin\beta_0 & \cos\beta_0 & 0 & 0 & 0 \\ 0 & 0 & 0 & 1 & 0 & 0 \\ 0 & 0 & 0 & 0 & \cos\beta_0 & \sin\beta_0 \\ 0 & 0 & 0 & 0 & -\sin\beta_0 & \cos\beta_0 \end{bmatrix} \cdot [-\boldsymbol{I}_{6\times6},\ \boldsymbol{I}_{6\times6}], \tag{20}$$

where $\boldsymbol{K}_{\mathrm{Sup},O^rX^rY^rZ^r}$ is the support-stiffness matrix in $O^rX^rY^rZ^r$, $\boldsymbol{T}_1$ is the transfer matrix from $o^dx^dy^dz^d$ to $O^rX^rY^rZ^r$, and $\boldsymbol{I}_{6\times6}$ is the 6 × 6 identity matrix.

In terms of the Shell181 model shown in Fig. 5(b), the left end should be rigid with the help of the "CERIG" command and Mass21 element in ANSYS to make the Matrix27 element available in simulating the elastic supports.

Figure 6 shows the first-five order dynamic frequency variations obtained from the proposed model, the Beam188 model, and the Shell181 model. Generally speaking, the results obtained from the three models agree well with each other. However, the torsional dynamic frequencies (see f_{n5} in Fig. 6) obtained from the proposed model are closer to those obtained from the Shell181 model rather than the Beam188 model. This is because the effect of the pre-twisted angle on the torsional stiffness in the Beam188 model is ignored [43]. In addition, the first-

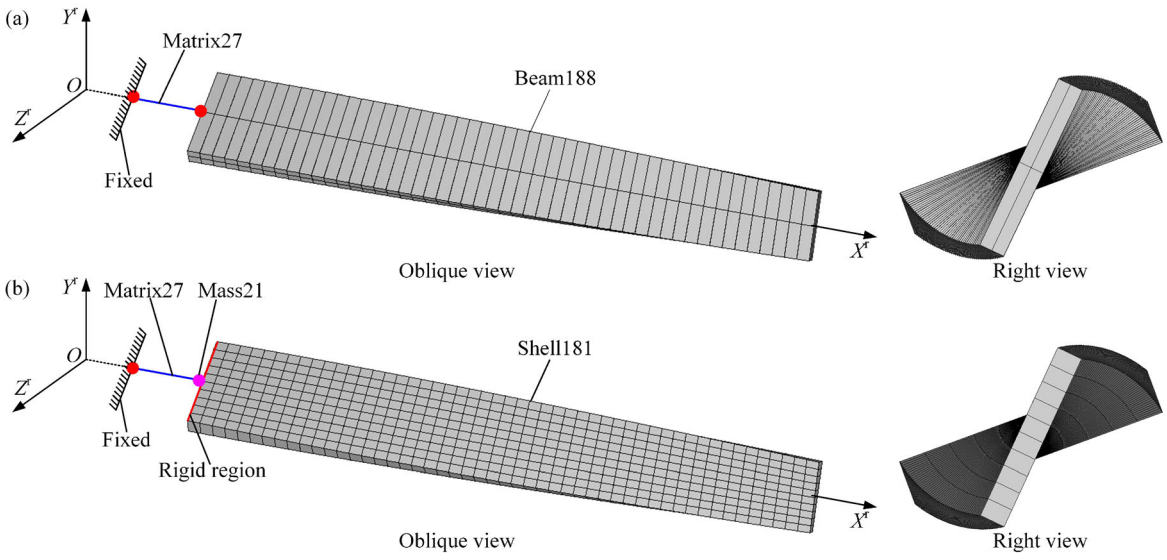

Fig. 5 Finite element model of a pre-twisted beam with elastic-support boundary: (a) Beam188 and (b) Shell181.

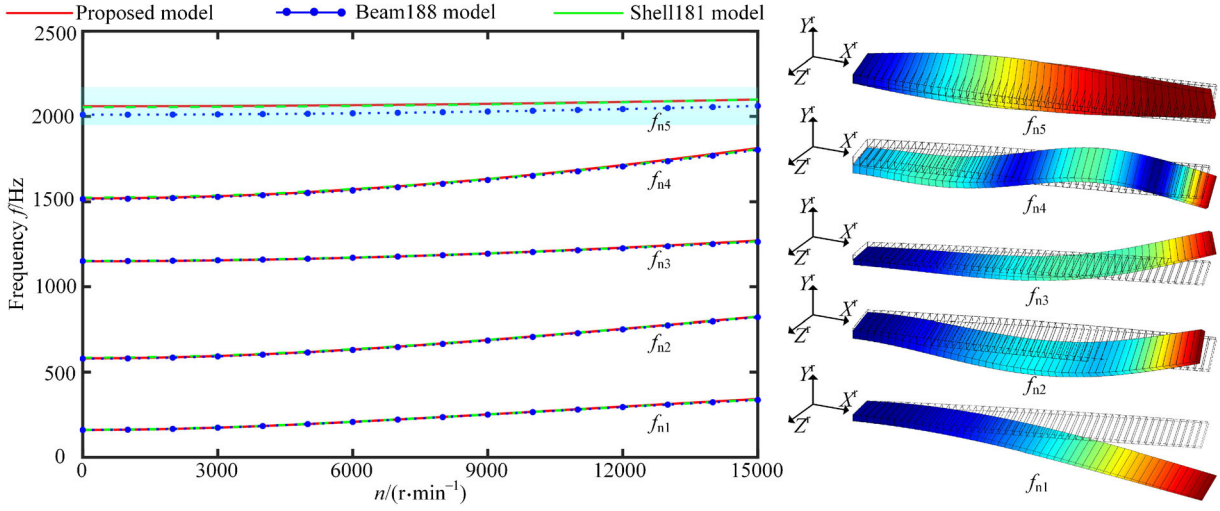

Fig. 6 First five-order dynamic frequencies and modal shapes.

five order modal shapes obtained from the proposed model under $n = 0$ r/min are also plotted in Fig. 6.

3 Analysis of modal coupling among y^d, z^d, and rotx^d vibrations

To quantify the degree of coupling among y^d, z^d, and rotx^d vibration modes varying with β_0, $\gamma(L)$, and n, the modal strain energy method is then adopted to determine the corresponding MSERs. The MSER in the x^d direction, that is, the axial direction, is inessential and ignored, which is because the x^d vibration mode is hard to be excited in most cases. In addition, the effect of $\ddot{\alpha}$ in Eqs. (8)–(13) is also ignored in this work. The QR method is used to solve Eq. (18) in order to obtain the rth corresponding right eigenvector $\boldsymbol{q}_r$ with a MATLAB program, that is,

$$\boldsymbol{M}\ddot{\boldsymbol{q}}_r + \boldsymbol{C}\dot{\boldsymbol{q}}_r + (\boldsymbol{K}_e + \boldsymbol{K}_c + \boldsymbol{K}_s + \boldsymbol{K}_{acc})\boldsymbol{q}_r = 0, \quad (21)$$

where $\boldsymbol{q}_r = [V_1, V_2, ..., V_N, W_1, W_2, ..., W_N, \Theta_1, \Theta_2, ..., \Theta_N, \Phi_1, \Phi_2, ..., \Phi_N, \Psi_1, \Psi_2, ..., \Psi_N]^T$.

Then, the MSER in the χ direction ($\chi = y^d$, z^d, or rotx^d) can be calculated using the following formula:

$$\mathrm{MSER}=\frac{\left\|\left(\boldsymbol{q}_r^{\chi}\right)^{\mathrm{T}}\left(\boldsymbol{K}_{\mathrm{e}}+\boldsymbol{K}_{\mathrm{c}}+\boldsymbol{K}_{\mathrm{s}}\right)_{\chi}\boldsymbol{q}_r^{\chi}\right\|}{\sum_{\chi=y^{\mathrm{b}},z^{\mathrm{b}},\mathrm{rot}x^{\mathrm{b}}}\left\|\left(\boldsymbol{q}_r^{\chi}\right)^{\mathrm{T}}\left(\boldsymbol{K}_{\mathrm{e}}+\boldsymbol{K}_{\mathrm{c}}+\boldsymbol{K}_{\mathrm{s}}\right)_{\chi}\boldsymbol{q}_r^{\chi}\right\|},\quad(22)$$

where $\boldsymbol{q}_r^{y^{\mathrm{d}}}=[V_1, V_2, \ldots, V_N, \Psi_1, \Psi_2, \ldots, \Psi_N]^{\mathrm{T}}$, $\boldsymbol{q}_r^{z^{\mathrm{d}}}=[W_1, W_2, \ldots, W_N, \Phi_1, \Phi_2, \ldots, \Phi_N]^{\mathrm{T}}$, $\boldsymbol{q}_r^{\mathrm{rot}x^{\mathrm{d}}}=[\Theta_1, \Theta_2, \ldots, \Theta_N]^{\mathrm{T}}$, and $(\boldsymbol{K}_{\mathrm{e}}+\boldsymbol{K}_{\mathrm{c}}+\boldsymbol{K}_{\mathrm{s}})_{\chi}$ represents the stiffness matrix in the χ direction.

3.1 Effects of β_0 on MSERs

Under the premise of $\gamma(L)=0°$, the MSERs in the y^{d}, z^{d}, and rotx^{d} directions under $\beta_0=0°$, 15°, 30°, and 45° are plotted in Fig. 7. As can be seen, the degree of coupling in the y^{d}, z^{d}, and rotx^{d} directions increase with increasing n and β_0 other than $\beta_0=0°$. The reason for this is due to the existence of Coriolis coupling, stiffness coupling, and mass coupling terms in Eqs. (9)–(13). Some main conclusions are made as follows:

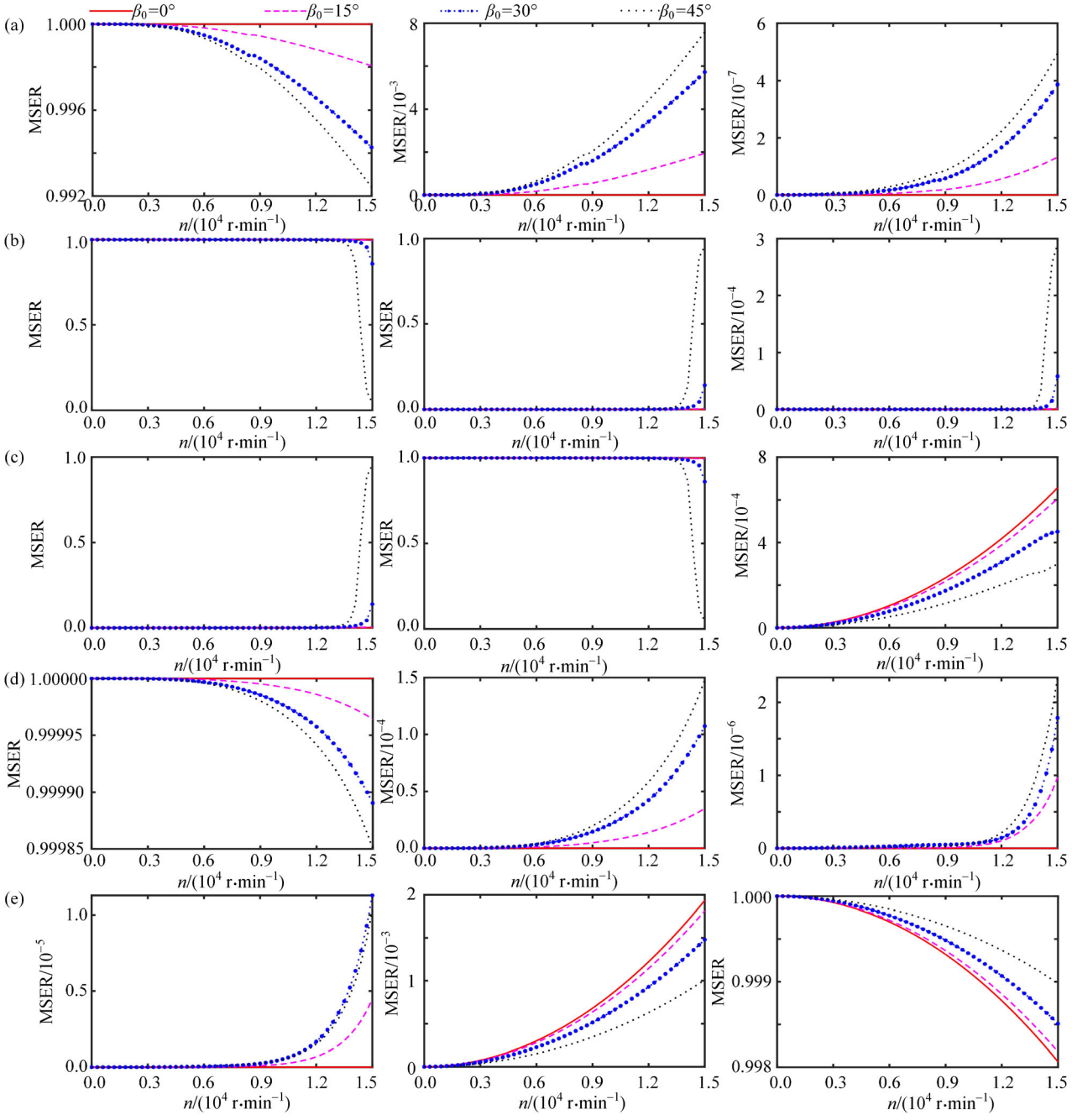

Fig. 7 Effects of β_0 on y^{d}, z^{d}, and rotx^{d} strain energy ratios varying with n: (a) $f_{\mathrm{n}1}$, (b) $f_{\mathrm{n}2}$, (c) $f_{\mathrm{n}3}$, (d) $f_{\mathrm{n}4}$, and (e) $f_{\mathrm{n}5}$. Note: The left column represents MSER in the y^{d} direction; the middle column represents MSER in the z^{d} direction; and the right column represents MSER in the rotx^{d} direction.

(1) When $\beta_0 = 0°$ and $n \neq 0$ r/min, the coupling terms between y^d and z^d and rotx^d directions do not exist (see $+0.5\int_0^L \rho A\dot{\alpha}^2 \sin(2\beta_0) W\delta V \mathrm{d}x$ in Eq. (9); $+2\int_0^L \rho\dot{\alpha}(I_y \sin\gamma \cdot\cos\beta - I_z \cos\gamma \sin\beta)\dot{\Theta}\delta\Psi \mathrm{d}x$, $+0.5\int_0^L \rho\,(I_y - I_z)\sin(2\gamma)\ddot{\Phi}\delta\Psi \cdot \mathrm{d}x$, $+\frac{1}{2}E\int_0^L \left(I_y - I_z\right)\sin(2\gamma)\Phi'\delta\Psi' \mathrm{d}x$, and $-0.5\int_0^L \rho\dot{\alpha}^2 (I_y - I_z)\sin(2\gamma)\Phi\delta\Psi \mathrm{d}x$ in Eq. (13); and Figs. 7(a), 7(b), and 7(d)), but the coupling term between z^d and rotx^d directions still exists, leading to the appearance of MSERs in both directions (see the Coriolis coupling term $-2\int_0^L \rho\dot{\alpha}(I_y \cos\gamma \cdot\cos\beta + I_z \sin\gamma \sin\beta)\dot{\Phi}\delta\Theta \mathrm{d}x$ in Eq. (11) and Figs. 7(c) and 7(e)). In particular, for the y^d-dominated modes, the MSERs in the z^d and rotx^d directions are zero due to the nonexistence of the displacement component in both directions, and vice versa (see Figs. 7(a), 7(b), and 7(d)). Similar patterns can also be found in the z^d-/rot^d-dominated modes (see Figs. 7(c) and 7(e)). Here, the modal shapes corresponding to Figs. 7(a)–7(e) under 0 r/min are plotted in Fig. 8.

(2) When $\beta_0 \neq 0°$ and $n \neq 0$ r/min, the degree of coupling among y^d, z^d, and rotx^d directions is dependent on the Coriolis coupling term $-2\int_0^L \rho\dot{\alpha}(I_y \cos\beta \sin\gamma - I_z \cos\gamma \cdot\sin\beta)\dot{\Psi}\delta\Theta \mathrm{d}x$ in Eq. (11) and the stiffness coupling term $+0.5\int_0^L \rho A\dot{\alpha}^2 \sin(2\beta_0) W\delta V \mathrm{d}x$ in Eq. (9). Obviously, the absolute values of these coupling terms increase with the increase of β_0 ($\beta_0 \in [0°, 45°]$). In other words, the degree of coupling among the y^d, z^d, and rotx^d directions is also gradually strengthened. More specifically, in terms of the flapwise-dominated modes (see Figs. 8(a), 8(b), and 8(d)), the MSERs in z^d and rotx^d directions are maximum, but the MSER in the y^d direction is minimum when $\beta_0 = 45°$. Similar rules are also suitable for the analysis of the flapwise- and torsional-dominated modes (see Figs. 7(c), 7(e), 8(c), and 8(e)).

(3) A larger n leads to a stronger degree of coupling among y^d, z^d, and rotx^d directions for the same β_0 (Figs. 7(a)–7(e)). This can be easily illustrated via the aforementioned conclusions (1) and (2), and no more expatiation is presented here.

3.2 Effects of $\gamma(L)$ on MSERs

Under the premise of $\beta_0 = 0°$, the MSERs in the y^d, z^d, and rotx^d directions under $\gamma(L) = 0°$, 15°, 30°, and 45° are shown in Fig. 9. Here, the effect of $\gamma(L) = 0°$ on MSERs has been explicitly analyzed in Subsection 3.1, and no more clarifications are made here. Obviously, the introduction of $\gamma(L)$ automatically leads to the structural coupling between y^d and z^d directions (see the mass coupling term $+0.5 \cdot \int_0^L \rho(I_y - I_z)\sin(2\gamma)\ddot{\Psi}\delta\Phi \mathrm{d}x$ and structural stiffness coupling term $+0.5E\int_0^L (I_y - I_z)\sin(2\gamma)\Psi'\delta\Phi' \mathrm{d}x$ in Eq. (12)). In addition, the introduction of n further causes the coupling among the y^d, z^d, and rotx^d directions (see the Coriolis coupling term $+2\int_0^L \rho\dot{\alpha}(I_y \cos\gamma\cos\beta + I_z \sin\gamma\sin\beta)\dot{\Phi}\delta\Theta \mathrm{d}x$ $-2\int_0^L \rho\dot{\alpha}(I_y \cos\beta\sin\gamma - I_z \cos\gamma\sin\beta)\dot{\Psi}\delta\Theta \mathrm{d}x$ in Eq. (11) and stiffness coupling term $+0.5\int_0^L \rho\dot{\alpha}^2 (I_z - I_y)\sin(2\gamma)\Psi\delta\Phi \mathrm{d}x$ in Eq. (12)). Some main conclusions are summarized as follows:

(1) In terms of flapwise-dominated modes (see Figs. 6, 9(a), 9(b), and 9(d)), MSER decreases in the y^d direction and increases in the z^d direction with increasing $\gamma(L)$, which indicates that the degree of coupling is increasingly strengthened. This can be attributed to the enhanced coupling effects such as mass coupling in Eq. (11) and stiffness coupling in Eqs. (11) and (12). In addition, the MSER in the rotx^d direction comes from the two coupling contributions in both y^d and z^d directions (see the Coriolis coupling term $+2\int_0^L \rho\dot{\alpha}(I_y \cos\gamma\cos\beta + I_z \sin\gamma\sin\beta)\dot{\Phi}\delta\Theta \mathrm{d}x$ $-2\int_0^L \rho\dot{\alpha}(I_y \cos\beta\sin\gamma - I_z \cos\gamma\sin\beta)\dot{\Psi}\delta\Theta \mathrm{d}x$ in Eq. (11)). The coupling contribution coming from the y^d direction increases, but those coming from the z^d direction decrease with increasing $\gamma(L)$, causing the non-monotonic change of rotx^d MSER under the combined effect of y^d and z^d MSER

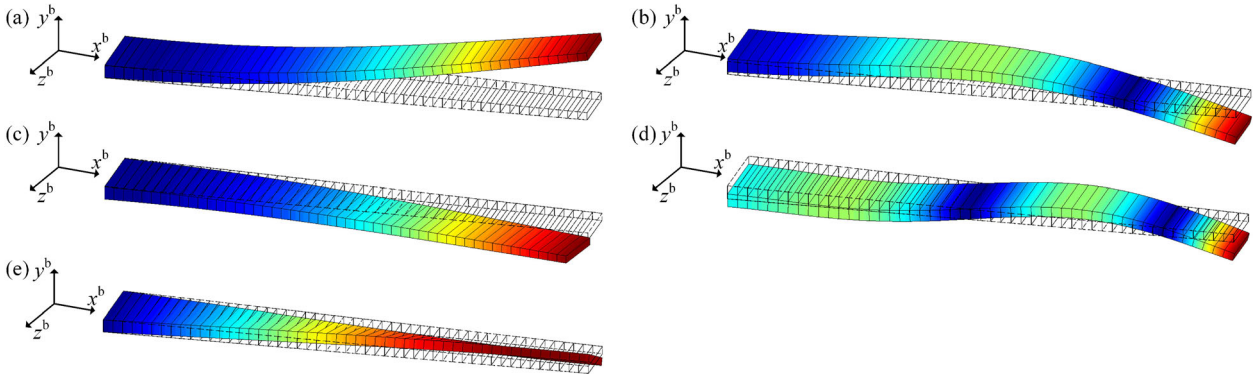

Fig. 8 First five-order modal shapes under $n = 0$ r/min: (a) f_{n1}, (b) f_{n2}, (c) f_{n3}, (d) f_{n4}, and (e) f_{n5}.

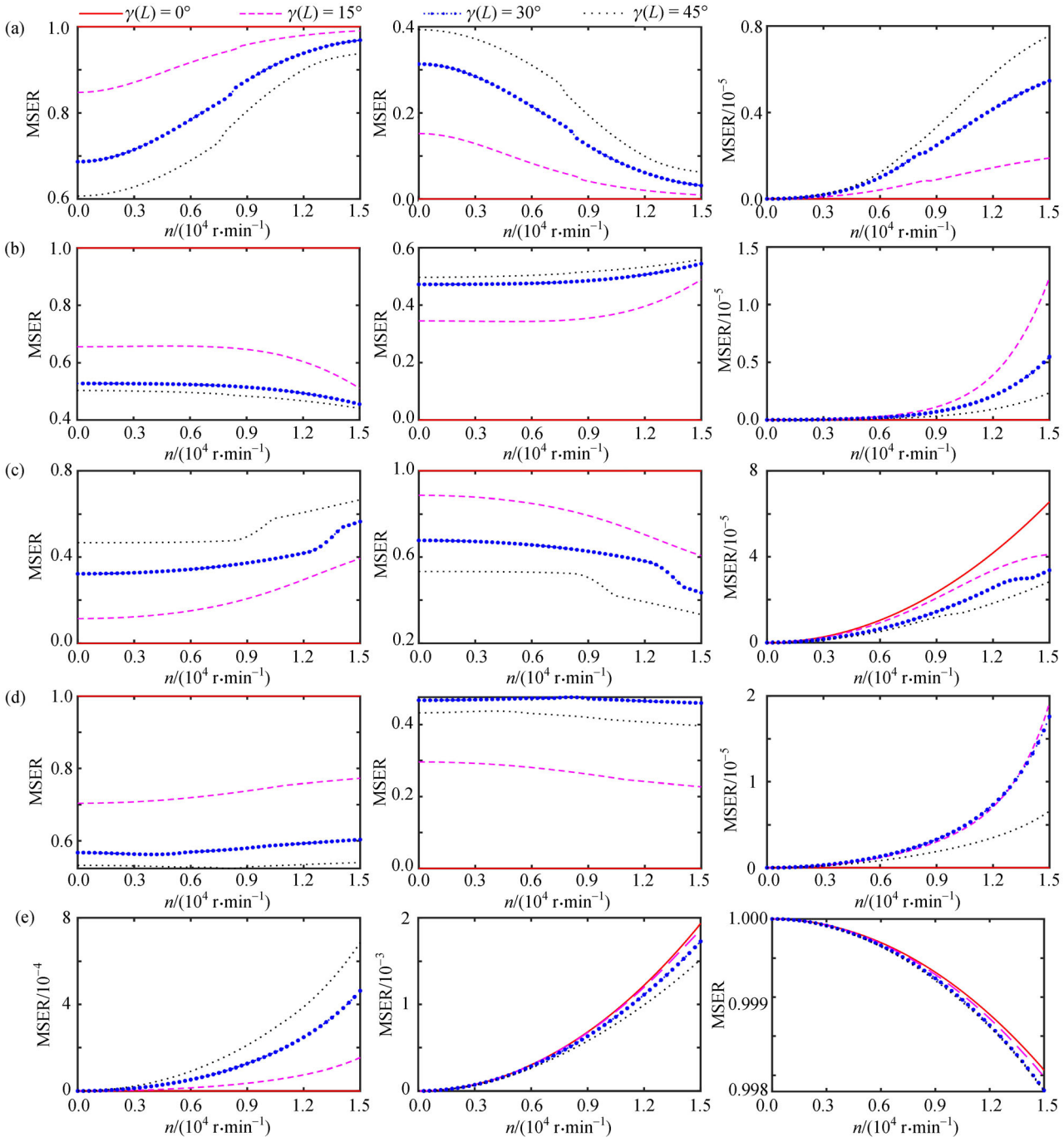

Fig. 9 Effects of $\gamma(L)$ on y^{d}, z^{d}, and rotx^{d} strain energy ratios varying with n: (a) f_{n1}, (b) f_{n2}, (c) f_{n3}, (d) f_{n4}, and (e) f_{n5}. Note: The left column represents MSER in the y^{d} direction; the middle column represents MSER in the z^{d} direction; and the right column represents MSER in the rotx^{d} direction.

(see Figs. 9(a), 9(b), and 9(d)). Similar rules also exist in the flapwise-dominated modes (see Figs. 6 and 9(c)) and need not be repeated here.

(2) In terms of torsional-dominated mode (see Figs. 6 and 9(e)), the MSER in the rotx^{d} direction decreases with increasing $\gamma(L)$, whereas those in the y^{d} and z^{d} directions increase and decrease with increasing $\gamma(L)$, respectively, which is mainly due to the strengthened coupling effect in the y^{d} direction (see the Coriolis coupling term $-2\cdot\int_0^L\rho\dot{\alpha}(I_y\cos\beta\sin\gamma-I_z\cos\gamma\sin\beta)\dot{\Psi}\delta\Theta\mathrm{d}x$ in Eq. (11)) and the degraded coupling effect in the z^{d} direction (see the Coriolis coupling term $-2\int_0^L\rho\dot{\alpha}(I_y\cos\gamma\sin\beta+I_z\sin\gamma\sin\beta)\cdot\dot{\Phi}\delta\Theta\mathrm{d}x$ in Eq. (11)).

(3) For the flapwise-/chordwise-dominated mode (see Figs. 6 and 9(a)–9(d)), the MSERs in the y^{d} and z^{d} directions are complementary in the changing trend and close to 1 with increasing n for the same $\gamma(L)$, whereas those for the torsional-dominated mode (see Figs. 6 and 9(e)) are the same in the changing trend.

4 Conclusions

In this work, Hamilton's principle in combination with assumed mode method is adopted to establish the coupled flapwise–chordwise–axial–torsional dynamic model of a rotating double-tapered, pre-twisted, and inclined Timoshenko beam with elastically restrained root. Then, the proposed model is verified by comparing natural characteristics obtained from the experiment and ANSYS models using Beam188 and Shell181 elements. Finally, the MSER is adopted to quantify the degree of coupling among the flapwise, chordwise, and torsional directions under the effects of setting angle, pre-twisted angle, and rotating speed. Some conclusions are made as follows:

(1) Both flapwise–torsional coupling and chordwise–torsional coupling are determined via the Coriolis coupling term. The degrees of flapwise–torsional coupling and chordwise-torsional coupling increase and decrease with increasing setting and pre-twisted angles, respectively. The changing trend of MSER in the torsional direction is dependent on the combined effect of the flapwise–torsional and chordwise–torsional couplings, especially for flapwise-dominated or chordwise-dominated mode.

(2) The pre-twisted angle has more effect on the degree of flapwise–chordwise coupling than the setting angle, thereby inducing stronger mode coupling. The introduction of pure setting angle only causes one stiffness coupling term related to the rotating speed, whereas the introduction of the pure pre-twisted angle not only leads to the stiffness coupling term related to the rotating speed but also the structural stiffness and mass couplings independent on the rotating speed.

Nomenclature

A	Area of an arbitrary beam section
$\boldsymbol{A}_1$, $\boldsymbol{A}_2$, $\boldsymbol{A}_3$, $\boldsymbol{A}_4$, $\boldsymbol{A}_5$	Transfer matrices from *oxyz* to *OXYZ*
b_0	Beam root width
$\boldsymbol{C}$	Coriolis matrix
E	Young's modulus
$\boldsymbol{F}$	External force vector
G	Shear modulus
h_0	Beam root thickness
I_y, I_z	Second moment of area in the *y*- and *z*-axes, respectively
J	Torsional moment of inertia
k_x, k_y, k_z, k_{rx}, k_{ry}, k_{rz}	Linear and angular support stiffness in $o^{\mathrm{d}}x^{\mathrm{d}}y^{\mathrm{d}}z^{\mathrm{d}}$
$\boldsymbol{K}_{\mathrm{e}}$, $\boldsymbol{K}_{\mathrm{c}}$, $\boldsymbol{K}_{\mathrm{s}}$, $\boldsymbol{K}_{\mathrm{acc}}$	Structural, centrifugal stiffening, spin softening, and angular acceleration-induced stiffness matrices, respectively
L	Beam length
$\boldsymbol{M}$	Mass matrix
n	Rotating speed
N	Modal truncation number
oxyz	Local coordinate system located at the arbitrary beam section
$o^{\mathrm{d}}x^{\mathrm{d}}y^{\mathrm{d}}z^{\mathrm{d}}$	Local coordinate system attached to the joint surface on the disk
OXYZ	Global coordinate system
$O^{\mathrm{r}}X^{\mathrm{r}}Y^{\mathrm{r}}Z^{\mathrm{r}}$	Rotating coordinate system
$\boldsymbol{q}$, $\boldsymbol{Q}$	Displacement vectors in *oxyz* and $o^{\mathrm{d}}x^{\mathrm{d}}y^{\mathrm{d}}z^{\mathrm{d}}$, respectively
$\boldsymbol{q}_r$	The rth right eigenvector
$\boldsymbol{r}_p$, $\dot{\boldsymbol{r}}_p$	Coordinate and velocity vectors, respectively
R_{d}	Disk radius
t	Time
T_{b}	Kinetic energy
u, v, w; U, V, W	Linear displacement components in *oxyz* and $o^{\mathrm{d}}x^{\mathrm{d}}y^{\mathrm{d}}z^{\mathrm{d}}$, respectively
U_{b}	Potential energy
$U_i(t)$, $V_i(t)$, $W_i(t)$	The ith-mode canonical coordinates related to U, V, and W
U', V', W'	Linear displacements differentiating with respect to x
X^p, Y^p, Z^p; x, y, z	Coordinates of an arbitrary point "p" on the beam section in *OXYZ* and *oxyz*, respectively
Θ, Φ, Ψ	Angular displacements $o^{\mathrm{d}}x^{\mathrm{d}}y^{\mathrm{d}}z^{\mathrm{d}}$
Θ', Φ', Ψ'	Angular displacements differentiating with respect to x
$\Theta_i(t)$, $\Phi_i(t)$, $\Psi_i(t)$	The ith-mode canonical coordinates related to Θ, Φ, Ψ
α, $\dot{\alpha}$	Angular displacement and angular velocity, respectively
β, β_0	Setting angles of the arbitrary and root sections, respectively
$\beta_{\mathrm{a}i}$, $\beta_{\mathrm{f}i}$, $\beta_{\mathrm{c}i}$, $\beta_{\mathrm{t}i}$	Characteristic roots
γ, $\gamma(L)$	Pre-twisted angles of the arbitrary and tip sections, respectively
δ	Variation symbol
θ, ϕ, ψ	Angular displacements in *oxyz*
κ_y, κ_z	Shear factors along the *y*- and *z*-directions, respectively
$\xi_{\mathrm{f}i}$, $\xi_{\mathrm{c}i}$	Coefficients related to $\beta_{\mathrm{f}i}$ and $\beta_{\mathrm{c}i}$
ρ	Density
τ_{h}, τ_{b}	Tapered ratio of thickness and width, respectively
ν	Poisson's ratio
ϕ_{ji}	Assumed mode shapes
MSER	Modal strain energy ratio

Acknowledgements This project was supported by the National Natural Science Foundation (Grant Nos. 11972112 and 11772089), the Fundamental Research Funds for the Central Universities (Grant Nos. N170308028, N170306004, N2003014, and N180708009), and Liaoning Revitalization Talents Program (Grant No. XLYC1807008).

References

1. Lin S M. Dynamic analysis of rotating nonuniform Timoshenko beams with an elastically restrained root. Journal of Applied Mechanics, 1999, 66(3): 742–749
2. He Q, Xuan H J, Liu L L, et al. Perforation of aero-engine fan casing by a single rotating blade. Aerospace Science and Technology, 2013, 25(1): 234–241
3. Javdani S, Fabian M, Carlton J S, et al. Underwater free-vibration analysis of full-scale marine propeller using a fiber Bragg grating-based sensor system. IEEE Sensors Journal, 2016, 16(4): 946–953
4. Rezaei M M, Behzad M, Haddadpour H, et al. Development of a reduced order model for nonlinear analysis of the wind turbine blade dynamics. Renewable Energy, 2015, 76: 264–282
5. Rao J S, Carnegie W. Solution of the equations of motion of coupled-bending bending torsion vibrations of turbine blades by the method of Ritz–Galerkin. International Journal of Mechanical Sciences, 1970, 12(10): 875–882
6. Houbolt J C, Brooks G W. Differential equations of motion for combined flapwise bending, chordwise bending, and torsion of twisted nonuniform rotor blades. National Advisory Committee for Aeronautics, Technical Note 3905, 1957
7. Du H, Lim M K, Liew K M. A power series solution for vibration of a rotating Timoshenko beam. Journal of Sound and Vibration, 1994, 175(4): 505–523
8. Rao J S. Flexural vibration of pretwisted tapered cantilever blades. Journal of Engineering for Industry, 1972, 94(1): 343–346
9. Şakar G, Sabuncu M. Dynamic stability of a rotating asymmetric cross-section blade subjected to an axial periodic force. International Journal of Mechanical Sciences, 2003, 45(9): 1467–1482
10. Banerjee J R. Free vibration of centrifugally stiffened uniform and tapered beams using the dynamic stiffness method. Journal of Sound and Vibration, 2000, 233(5): 857–875
11. Zeng J, Ma H, Yu K, et al. Rubbing response comparisons between single blade and flexible ring using different rubbing force models. International Journal of Mechanical Sciences, 2019, 164: 105164
12. Zeng J, Zhao C G, Ma H, et al. Rubbing dynamic characteristics of the blisk-casing system with elastic supports. Aerospace Science and Technology, 2019, 95: 105481
13. Hodges D H, Dowell E H. Nonlinear equations of motion for the elastic bending and torsion of twisted nonuniform rotor blades. NASA Technical Report NASA-TN-D-7818, A-5711, 1974
14. Zhu T L. The vibrations of pre-twisted rotating Timoshenko beams by the Rayleigh–Ritz method. Computational Mechanics, 2011, 47(4): 395–408
15. Ma H, Xie F T, Nai H Q, et al. Vibration characteristics analysis of rotating shrouded blades with impacts. Journal of Sound and Vibration, 2016, 378: 92–108
16. Xie F T, Ma H, Cui C, et al. Vibration response comparison of twisted shrouded blades using different impact models. Journal of Sound and Vibration, 2017, 397: 171–191
17. Sinha S K. Combined torsional-bending-axial dynamics of a twisted rotating cantilever Timoshenko beam with contact-impact loads at the free end. Journal of Applied Mechanics, 2007, 74(3): 505–522
18. Yang X D, Wang S W, Zhang W, et al. Dynamic analysis of a rotating tapered cantilever Timoshenko beam based on the power series method. Applied Mathematics and Mechanics, 2017, 38(10): 1425–1438
19. Şakar G, Sabuncu M. Buckling and dynamic stability of a rotating pretwisted asymmetric cross-section blade subjected to an axial periodic force. Finite Elements in Analysis and Design, 2004, 40(11): 1399–1415
20. Sabuncu M, Evran K. Dynamic stability of a rotating pre-twisted asymmetric cross-section Timoshenko beam subjected to an axial periodic force. International Journal of Mechanical Sciences, 2006, 48(6): 579–590
21. Subrahmanyam K B, Kaza K R V, Brown G V, et al. Nonlinear bending-torsional vibration and stability of rotating, pretwisted, preconed blades including Coriolis effects. In: Proceedings of Workshop on Dynamics and Aeroelastic Stability Modeling of Rotor Systems. Atlanta: NASA, 1986, NASA-TM-87207
22. Sina S A, Haddadpour H. Axial–torsional vibrations of rotating pretwisted thin walled composite beams. International Journal of Mechanical Sciences, 2014, 80: 93–101
23. Adair D, Jaeger M. Vibration analysis of a uniform pre-twisted rotating Euler–Bernoulli beam using the modified Adomian decomposition method. Mathematics and Mechanics of Solids, 2018, 23(9): 1345–1363
24. Oh Y, Yoo H H. Vibration analysis of a rotating pre-twisted blade considering the coupling effects of stretching, bending, and torsion. Journal of Sound and Vibration, 2018, 431: 20–39
25. Lee J W, Lee J Y. Development of a transfer matrix method to obtain exact solutions for the dynamic characteristics of a twisted uniform beam. International Journal of Mechanical Sciences, 2016, 105: 215–226
26. Banerjee J R. Development of an exact dynamic stiffness matrix for free vibration analysis of a twisted Timoshenko beam. Journal of Sound and Vibration, 2004, 270(1–2): 379–401
27. Subrahmanyam K B, Kaza K R V. Vibration and buckling of rotating, pretwisted, preconed beams including Coriolis effects. Journal of Vibration and Acoustics, 1986, 108(2): 140–149
28. Hashemi S M, Richard M J. Natural frequencies of rotating uniform beams with Coriolis effects. Journal of Vibration and Acoustics, 2001, 123(4): 444–455
29. Banerjee J R, Kennedy D. Dynamic stiffness method for inplane free vibration of rotating beams including Coriolis effects. Journal of Sound and Vibration, 2014, 333(26): 7299–7312
30. Oh S Y, Song O, Librescu L. Effects of pretwist and presetting on coupled bending vibrations of rotating thin-walled composite beams. International Journal of Solids and Structures, 2003, 40(5): 1203–1224
31. Latalski J, Warminski J, Rega G. Bending–twisting vibrations of a rotating hub–thin-walled composite beam system. Mathematics and Mechanics of Solids, 2017, 22(6): 1303–1325
32. Ondra V, Titurus B. Free vibration analysis of a rotating pre-twisted beam subjected to tendon-induced axial loading. Journal of Sound

and Vibration, 2019, 461: 114912
33. Zeng J, Chen K K, Ma H, et al. Vibration response analysis of a cracked rotating compressor blade during run-up process. Mechanical Systems and Signal Processing, 2019, 118: 568–583
34. Sun Q, Ma H, Zhu Y P, et al. Comparison of rubbing induced vibration responses using varying-thickness-twisted shell and solid-element blade models. Mechanical Systems and Signal Processing, 2018, 108: 1–20
35. Ma H, Wang D, Tai X Y, et al. Vibration response analysis of blade-disk dovetail structure under blade tip rubbing condition. Journal of Vibration and Control, 2017, 23(2): 252–271
36. Lin S M. The instability and vibration of rotating beams with arbitrary pretwist and an elastically restrained root. Journal of Applied Mechanics, 2001, 68(6): 844–853
37. Lin S M, Wu C T, Lee S Y. Analysis of rotating nonuniform pretwisted beams with an elastically restrained root and a tip mass. International Journal of Mechanical Sciences, 2003, 45(4): 741–755
38. Lee S Y, Lin S M, Wu C T. Free vibration of a rotating non-uniform beam with arbitrary pretwist, an elastically restrained root and a tip mass. Journal of Sound and Vibration, 2004, 273(3): 477–492
39. Choi S T, Chou Y T. Vibration analysis of elastically supported turbomachinery blades by the modified differential quadrature method. Journal of Sound and Vibration, 2001, 240(5): 937–953
40. Bambill D V, Rossit C A, Rossi R E, et al. Transverse free vibration of non uniform rotating Timoshenko beams with elastically clamped boundary conditions. Meccanica, 2013, 48(6): 1289–1311
41. Digilov R M, Abramovich H. The impact of root flexibility on the fundamental frequency of a restrained cantilever beam. International Journal of Mechanical Engineering Education, 2017, 45(2): 184–193
42. Hodges D H. Torsion of pretwisted beams due to axial loading. Journal of Applied Mechanics, 1980, 47(2): 393–397
43. Zeng J, Ma H, Yu K, et al. Coupled flapwise-chordwise-axial-torsional dynamic responses of rotating pre-twisted and inclined cantilever beams subject to the base excitation. Applied Mathematics and Mechanics, 2019, 40(8): 1053–1082